

Large flux-mediated coupling in hybrid electromechanical system with a transmon qubit

Tanmoy Bera,¹ Sourav Majumder,¹ Sudhir Kumar Sahu,¹ and Vibhor Singh^{1,*}

¹*Department of Physics, Indian Institute of Science, Bangalore-560012 (India)*

(Dated: February 8, 2022)

Control over the quantum states of a massive oscillator is important for several technological applications and to test the fundamental limits of quantum mechanics. Addition of an internal degree of freedom to the oscillator could be a valuable resource for such control. Recently, hybrid electromechanical systems using superconducting qubits, based on electric-charge mediated coupling, have been quite successful. Here, we realize a hybrid device, consisting of a superconducting transmon qubit and a mechanical resonator coupled using the magnetic-flux. The coupling stems from the quantum-interference of the superconducting phase across the tunnel junctions. We demonstrate a vacuum electromechanical coupling rate up to 4 kHz by making the transmon qubit resonant with the readout cavity. Consequently, thermal-motion of the mechanical resonator is detected by driving the hybridized-mode with mean-occupancy well below one photon. By tuning qubit away from the cavity, electromechanical coupling can be enhanced to 40 kHz. In this limit, a small coherent drive on the mechanical resonator results in the splitting of qubit spectrum, and we observe interference signature arising from the Landau–Zener–Stückelberg effect. With improvements in qubit coherence, this system offers a novel platform to realize rich interactions and could potentially provide full control over the quantum motional states.

Cavity optomechanical systems, where a mechanical mode parametrically modulates the resonant frequency of an electromagnetic (EM) mode, have been very successful in controlling the motional states of massive oscillators [1]. Starting from the earlier demonstration of the motional quantum ground state by the sideband cooling technique [2, 3], these experiments have reached several milestones related to the displacement-detection [4] and the preparation of the non-classical states of mechanical motion [5, 6]. Beyond the traditional two-mode systems, consisting of one EM and one mechanical mode, cavity optomechanical systems with an auxiliary mode provides a wide range of interactions. Such systems have been used to realize nonreciprocal devices [7–9], and to demonstrate quantum entanglement between two mechanical resonators [10, 11].

Among the two-mode cavity optomechanical devices, preparation of the quantum states of motion appears to be technologically challenging. One successful strategy in the microwave domain, to circumvent this, is to introduce an auxiliary nonlinear mode such as a qubit. The qubit can be used as a single-photon source [12], photon-counter [13], or directly coupled to a mechanical mode using its charge dispersion [14–17] or the piezo-electric effect [18–20]. In such devices, the qubit mode ‘acts’ like an additional degree of freedom which couples to mechanical mode via an intermediate mode or directly using the “charge” dispersion.

While systems utilizing the charge-based coupling have been studied extensively, the experimental progress of the hybrid systems based on magnetic-flux has been very limited. Here we design and study the performance of a hybrid electromechanical device based on a fundamentally different coupling scheme based on the magnetic

flux. We engineer the device parameters such that in addition to the flux-based electromechanical coupling, one mode maintains sufficient anharmonicity to be qualified as a qubit. This approach results in an electromechanical system with an internal spin-half degree of freedom. While, the strong and tunable nonlinearity of the qubit mode improves the displacement sensitivity, the large electromechanical coupling also manifests in the modification of qubit spectrum in the dispersive limit. Similar to vacuum-electromechanical coupling rate’s scaling with total charge in charge-dispersion based schemes [14–16], the coupling rate with flux-based scheme is expected to scale linearly with the magnetic field. Therefore, such an approach has the potential to reach the elusive single-photon strong coupling regime with suitable choice of materials [21].

The hybrid device consists of a transmon qubit coupled to a mechanical resonator and a readout cavity, as shown in Fig. 1(a). The transmon qubit couples to the cavity via a dipole coupling, commonly referred to as transverse coupling, as it connects the ground and the first excited state of the qubit [22]. The mechanical resonator couples to the qubit via a flux-mediated coupling. Such coupling is achieved by embedding a mechanical resonator into one of the arms of a SQUID (Superconducting Quantum Interference Device) loop, which provides the necessary Josephson inductance to form a transmon qubit. Due to the quantum interference of the superconducting phase, the Josephson inductance of the SQUID depends on the magnetic flux threading the loop as schematically shown in Fig. 1(b). In the presence of a magnetic field applied normal to the plane of the SQUID, it acts like a displacement-dependent nonlinear inductor. By shunting the SQUID “inductor” to a suitable capacitance, a trans-

mon qubit mode can be designed. As the motion of the mechanical resonator directly affects the qubit transition frequency, this coupling is referred to as longitudinal coupling. A flux-coupled hybrid system formed this way can be thought of a dual to the “charge” coupling approach realized with the CPB qubit [16].

Theoretically, the flux-mediated electromechanical coupling has been considered in the context of flux-qubits [23], cavity-electromechanical devices [24], and more recently with the transmon qubit [21, 25]. On the experimental side, the scheme has been used for large bandwidth displacement detection [26], and to demonstrate the cavity-electromechanical system by embedding Josephson elements in the microwave circuitry [27, 28].

In comparison to existing flux-coupling approaches [27, 28], our design methodology circumvents several issues by using a tunable transmon-mode. First, the requirement of large Josephson inductance for transmon design helps in suppressing hysteretic effects with magnetic flux arising from geometrical and kinetic inductance. Second, our approach here is to implement a longitudinal coupling between transmon qubit and a mechanical resonator through the modulation of Josephson inductance. This enables the interaction of the mechanical mode with the qubit in two distinct ways. First, due to strong coupling between the qubit and cavity in the resonant limit, the mechanical motion directly couples to the hybridized-states. Second, in the dispersive limit when the qubit is detuned far away from the cavity, a sufficiently large coupling between the qubit and the mechanical mode can be maintained. It thus provides a mean to use the qubit as an internal degree of freedom to the mechanical mode and further paves ways for measurement-based cooling and control protocols [25, 29, 30].

Device design

We use a three-dimensional (3D) cavity to implement the transmon design as shown schematically in Fig. 1(c). Unlike the conventional 3D-transmon qubit, which couples differentially to the cavity mode, we design a single-ended qubit mode by grounding one end of the SQUID loop to the cavity wall using a small wirebond [31]. The other end of the SQUID loop extends towards the center of the cavity and provides the necessary qubit capacitance and coupling with the fundamental cavity mode. The rectangular cavity ($35 \times 4 \times 35$ mm³) is machined using OFHC copper with the fundamental resonant mode TE₁₀₁ at $\omega_c \approx 2\pi \times 6$ GHz. A false-color SEM image of the SQUID loop is shown in Fig. 1(d). The nanobeam-shaped mechanical resonator, formed by 100 nm highly-stressed SiN film coated with 50 nm of Aluminum, and suspended part of the Josephson junctions can be clearly seen. See supplementary information (SI) for details. The offset in the SQUID position (away from the cen-

ter of the cavity) in transmon design allows us to bring a RF drive line for the electrostatic actuation of the mechanical resonator (see SI for design simulations).

The transmon qubit frequency ω_q is given by $\hbar\omega_q \approx \sqrt{8E_C E_J^0} |\cos(\pi\Phi/\Phi_0)| - E_C$, where E_J^0 is the maximum Josephson energy, E_C is the charging energy, Φ is the total flux threading the SQUID loop, and $\Phi_0 = h/2e$ is the magnetic flux quanta. The tunability of qubit frequency with flux allows access to its dispersive or resonant interaction with the cavity. The interaction between the qubit and the cavity mode can be expressed as $\hbar J(\hat{a}\hat{\sigma}^+ + \hat{a}^\dagger\hat{\sigma}^-)$, where $\hat{a}(\hat{\sigma}^-)$ is the ladder operator for the cavity(qubit) mode and J is the dipole coupling rate. The electromechanical coupling arises from the modulation of qubit frequency caused by mechanical displacement. As the qubit frequency can be tuned over a large range, it is convenient to define the vacuum electromechanical coupling rate between the qubit-cavity hybridized states (ω_\pm) and the mechanical resonator as,

$$g_\pm(\Phi) = \frac{\partial\omega_\pm(\Phi)}{\partial x} x_{zp} = \Phi G_\Phi^\pm \frac{x_{zp}}{w}, \quad (1)$$

where $G_\Phi^\pm = \partial\omega_\pm(\Phi)/\partial\Phi$ is the flux-responsivity, x_{zp} is the quantum zero-point fluctuations of the mechanical resonator, and w is the effective width of the SQUID loop. Eq. 1 defines the coupling rate over the entire range of qubit frequencies. The hybridized modes $\omega_\pm = \bar{\Delta} \pm \sqrt{(\Delta/2)^2 + J^2}$ with $\Delta = \omega_q - \omega_c$ $\bar{\Delta} = (\omega_q + \omega_c)/2$ approach the uncoupled qubit and cavity frequencies in the dispersive limit. Restricting the coupled qubit-cavity system to single excitation subspace, in the resonant limit $\Delta \ll J$, the hybridized-modes essentially act like independent cavity optomechanical systems. However, it is worth pointing out here that the interaction between the hybridized modes and the mechanical motion can be used to enhance the quantum nonlinearity by designing J comparable to the mechanical frequency [32, 33].

Qubit spectroscopy and flux-responsivity

We use spectroscopic measurements to characterize the qubit. Fig. 2(a) shows the transmission ($|S_{21}(\omega)|$) through the cavity as applied magnetic flux is varied (see SI for details of the measurement setup). When the qubit becomes resonant with the cavity, the vacuum Rabi splitting is observed which signifies the strong coupling between the qubit and cavity mode. We determine a dipole coupling rate $J = 2\pi \times 85$ MHz, the bare cavity frequency $\omega_c = 2\pi \times 5.993$ GHz, maximum qubit frequency $\omega_q^0 = 2\pi \times 7.982$ GHz, and an anharmonicity of -132 MHz (see SI for details). Due to the flux-periodicity of qubit frequency, the vacuum-Rabi splitting pattern repeats with every new flux-quanta added. The extension panel of Fig. 2(a) shows the transmission measurement at a higher magnetic field. Apart from a small reduction

(~ 15 MHz) in the maximum qubit frequency and an increase in the dressed-cavity mode linewidth, we do not observe any significant change in the device parameters up to a field of ~ 3.7 mT ($310 \Phi_0$).

To understand the flux-transduction of hybridized-modes, we compute the flux-responsivity G_Φ^\pm using the measured qubit and cavity parameters and assuming identical junctions. Fig. 2(b) shows the plot of G_Φ^\pm with respect to the hybridized-mode frequencies. The flux-responsivity of the hybridized-modes increase as their relative detuning ($|\omega_\pm - \omega_c|$) increases. However, reduced transmission at frequencies far away from ω_c hinders their use for the mechanical transduction. We choose an optimum operating point of 6.025 GHz, corresponding to $G_\Phi^+/2\pi \sim 1.8$ GHz/ Φ_0 , for the mechanical resonator characterization. This flux-responsivity is significantly larger than the values reported with the SQUID cavity [27]. In addition, the flux-responsivity of qubit $G_\Phi^q = \partial\omega_q/\partial\Phi$ can be much larger near the half-integer flux quantum as shown in Fig. 2(c). In the dispersive limit, while the effective coupling between the dressed cavity and mechanical resonator degrades by a factor of $(J/\Delta)^2$, a large coupling between the qubit and the mechanical resonator can be maintained.

Detection of mechanical mode and vacuum electromechanical rate

We first focus on the driven response of the mechanical resonator. For electrostatic actuation, a weak ac signal and a dc voltage V_{dc} are applied at the mechanical drive port (see SI for details). We fine-tune the magnetic flux near $190 \Phi_0$ to operate the hybridized mode $\omega_+/2\pi$ at 6.025 GHz. We inject a microwave tone at ω_+ creating a mean photon occupation of ≈ 1 , calibrated independently using ac-Stark shift. The signal that emerges from the cavity is then mixed-down and recorded by a network analyzer. Fig. 3(a) shows the amplitude of the signal in a color plot as the mechanical drive frequency and V_{dc} are varied. The change in color over the background signifies the mechanical resonance. We measure the in-plane vibrational mode at $\omega_m \sim 2\pi \times 6.585$ MHz with a characteristic capacitive frequency softening with V_{dc} .

Next, we focus on the thermal motion of the mechanical resonator. We operate the hybridized mode at $\omega_+ = 2\pi \times 6.025$ GHz and drive the system with a microwave tone tuned to lower sideband ($\omega_+ - \omega_m$), creating a mean photon occupation of ~ 0.1 photons. The power spectral density (PSD) of the output signal is then recorded with a spectrum analyzer. The average PSD, along with the fitted Lorentzian is shown in Fig. 3(b). We measure a mechanical linewidth of $\gamma_m = 2\pi \times 6$ Hz, corresponding to a quality factor of $\sim 1.1 \times 10^6$.

For a drive at the lower sideband, the ratio of inte-

grated power at the up-converted frequency (P_m) near ω_+ to the power of transmitted carrier signal (P_d) at $\omega_+ - \omega_m$ can be conveniently expressed as $P_m/P_d = (2g_+/\kappa)^2 n_m^{th}$, where n_m^{th} is the mean thermal occupation of the mechanical mode, and κ is the hybridized-mode linewidth. By varying the fridge temperature, we estimated the mechanical mode to be thermalized to at least 50 mK or higher. For the calculation of g_+ , we use a thermal phonon occupancy of 169 corresponding to 53 mK (additional detail are given in SI). Fig. 3(c) shows the variation in g_+ as the magnetic flux through the SQUID loop is varied, while the hybridized-mode frequency is maintained fixed at $\omega_+/2\pi = 6.025$ GHz. The dotted line shows the expected electromechanical coupling rate estimated from Eq. 1 using the measured device parameters.

We emphasize that the vacuum electromechanical coupling rate of $g_+ \sim 2\pi \times 4$ kHz is limited by choice of ω_+ , and the magnetic field range available in our measurement setup. By operating at $\omega_c \pm J$, one can achieve the $G_\Phi^+/G_\Phi^q = 1/2$, resulting in $g_+ \sim 2\pi \times 15$ kHz. In addition, thin films of Al can withstand a larger magnetic field than the maximum field used here (3.7 mT). As the in-plane critical magnetic field is much larger than the perpendicular critical magnetic field for thin Al films, a configuration with field applied in-plane to the SQUID loop would result in significantly higher coupling rates for the out-of-plane mechanical mode.

Landau-Zener-Stückelberg interference in the dispersive limit

Next, we investigate the system by tuning the qubit away from ω_c . In the dispersive limit $|\Delta| \gg J$, the mechanics essentially decouples from the cavity mode. While the qubit-cavity interaction is given by $(J^2/\Delta) \hat{a}^\dagger \hat{a} \hat{\sigma}_z$, the longitudinal interaction between the uncoupled qubit and the mechanical resonator is given by $g_{qm} \hat{\sigma}_z (\hat{b} + \hat{b}^\dagger)$, where $g_{qm} = (\partial\omega_q/\partial x) x_{zp}$ is the qubit-electromechanical coupling rate and \hat{b} (\hat{b}^\dagger) is the lowering (raising) operator for the mechanical mode. With a superconducting qubit device, time-dependent longitudinal coupling scheme has been used to perform high-fidelity qubit measurements [34]. In the present device, a static g_{qm} would instead result in a small qubit-state dependent displacement ($\sim g_{qm} x_{zp}/\omega_m$) [29]. Here, we focus on the qubit dynamics while driving the mechanical resonator. The qubit is detuned to 4.9 GHz to enhance g_{qm} to 40 kHz, and its spectrum is probed using the two-tone spectroscopy technique. The mechanical resonator is coherently actuated at its resonant frequency. It is equivalent to the flux-modulation of the qubit frequency at ω_m , and a frequency deviation set by g_{qm} and the mechanical amplitude.

Fig. 4(a) shows the qubit spectrum as the strength of

mechanical drive is varied. We observe a splitting in the qubit spectrum with a weak modulation in-between. The separation between the primary splitting varies linearly with the mechanical amplitude. The primary splitting can be understood by considering the passage of the system across the region of avoided crossing with separation set by the strength of the spectroscopic tone (the Rabi-flop rate Ω_R) [35]. As the system moves across the avoided-crossing at a rate set by ω_m , the transition during multiple passages mix the two states, eventually resulting in almost equal population of the two energy levels. Hence, it results in the splitting of the qubit spectrum.

At large mechanical drive power, the system crosses avoided-crossing region with higher speed. In this regime, one would expect to see the interference fringes, arising from multiple Landau-Zener transitions, at a separation close to ω_m [35] (additional details are included in the SI). In our experiment, as the qubit linewidth is comparable to the modulation frequency ω_m , the fringes are not well resolved. Their signatures are visible as weak modulation between the primary splitting. We have performed numerical calculations based on the Lindblad master equation (details are included in SI). Fig. 4(b) shows the result from such calculations. Apart from capturing the linear amplitude dependence of the primary splitting, the calculated results show the weak modulation in the experimental data.

In summary, we have developed a hybrid electromechanical device by integrating a modified 3D-transmon qubit and extremely low loss mechanical resonator of SiN/Al. The detection of thermo-mechanical motion by driving the system with less than one photon highlights the large underlying coupling rate. Accessibility to different regimes of interaction is further demonstrated by the observation of the LZS interference. Looking ahead, by accessing in-plane vibration mode through changes in the design geometry and in combination with higher magnetic field, the flux coupling rate can be increased a lot. With further improvements in the coupling strength, the device in consideration can reach resolved sideband regime and strong coupling regime. This could enable experiments in the regime of the single-photon cooperativity exceeding one, and a conditional cooling of the mechanical resonator to the quantum ground state.

Methods

For device fabrication, we use an intrinsic Si (100) substrate coated with 100 nm thick high-stress SiN layer grown using the LPCVD method. Using standard lithography and shadow evaporation techniques, the transmon design is patterned in a single lithography step. To release the mechanical resonator, a combination of dry and wet etching processes is used. First, the exposed SiN is

vertically etched by the reactive ion etching using SF_6 and CHF_3 plasma. The aluminum film naturally acts as a mask layer and thus protects the SiN underneath it. In the second step of etching, a modified-TMAH based etchant is used to remove the exposed silicon, while providing excellent selectivity against Al and SiN (see SI for additional details). After the wet etch process, the samples are blow-dried gently with N_2 , requiring no critical point drying. The (111)-facets of Si resulted from the wet etch process can also be seen in Fig. 1(d). The sample placed inside a copper cavity, along with a small solenoid, is kept inside a cryoperm-shield to protect it from the ambient magnetic field fluctuations.

Acknowledgments

V.S. acknowledges the support received from Infosys Science Foundation, and under the “Early Career Research Award” by SERB, Department of Science and Technology (DST), Govt. of India. T. B. and S. M. thank Tata Trust for providing the travel support. The authors acknowledge device fabrication facilities at CeNSE, IISc, Bangalore, and central facilities at the Department of Physics funded by DST. Authors thank R. Vijayraghavan, Manas Kulkarni, Diptiman Sen, and G. S. Agarwal for valuable discussions.

Author contribution

T. B. and S. M. contributed equally to this work. V. S. conceived the experiments. T. B. and S. M. fabricated the devices. T. B., S. M. and S. K. S performed the measurements. T. B., S. M., and V. S. performed data analysis. All the authors contributed to write the manuscript and discuss the results.

* v.singh@iisc.ac.in

- [1] Aspelmeyer, M., Kippenberg, T. J., and Marquardt, F. *Reviews of Modern Physics* **86**(4), 1391–1452 December (2014).
- [2] Teufel, J. D., Donner, T., Li, D., Harlow, J. W., Allman, M. S., Cicak, K., Sirois, A. J., Whittaker, J. D., Lehnert, K. W., and Simmonds, R. W. *Nature* **475**(7356), 359–363 July (2011).
- [3] Chan, J., Alegre, T. P. M., Safavi-Naeini, A. H., Hill, J. T., Krause, A., Gröblacher, S., Aspelmeyer, M., and Painter, O. *Nature* **478**(7367), 89–92 October (2011).
- [4] Anetsberger, G., Gavartin, E., Arcizet, O., Unterreithmeier, Q. P., Weig, E. M., Gorodetsky, M. L., Kotthaus, J. P., and Kippenberg, T. J. *Physical Review A* **82**(6), 061804 December (2010).

- [5] Pirkkalainen, J.-M., Damskägg, E., Brandt, M., Massel, F., and Sillanpää, M. *Physical Review Letters* **115**(24), 243601 December (2015).
- [6] Wollman, E. E., Lei, C. U., Weinstein, A. J., Suh, J., Kronwald, A., Marquardt, F., Clerk, A. A., and Schwab, K. C. *Science* **349**(6251), 952–955 August (2015).
- [7] Peterson, G., Lecocq, F., Cicak, K., Simmonds, R., Aumentado, J., and Teufel, J. *Physical Review X* **7**(3), 031001 July (2017).
- [8] Bernier, N. R., Tóth, L. D., Koottandavida, A., Ioannou, M. A., Malz, D., Nunnenkamp, A., Feofanov, A. K., and Kippenberg, T. J. *Nature Communications* **8**(1), 604 September (2017).
- [9] Barzanjeh, S., Wulf, M., Peruzzo, M., Kalaei, M., Dieterle, P. B., Painter, O., and Fink, J. M. *Nature Communications* **8**(1), 1–7 October (2017).
- [10] Riedinger, R., Wallucks, A., Marinković, I., Löschner, C., Aspelmeyer, M., Hong, S., and Gröblacher, S. *Nature* **556**(7702), 473–477 April (2018).
- [11] Ockeloen-Korppi, C. F., Damskägg, E., Pirkkalainen, J.-M., Asjad, M., Clerk, A. A., Massel, F., Woolley, M. J., and Sillanpää, M. A. *Nature* **556**(7702), 478–482 April (2018).
- [12] Reed, A. P., Mayer, K. H., Teufel, J. D., Burkhardt, L. D., Pfaff, W., Reagor, M., Sletten, L., Ma, X., Schoelkopf, R. J., Knill, E., and Lehnert, K. W. *Nature Physics* **13**(12), 1163–1167 December (2017).
- [13] Lecocq, F., Teufel, J. D., Aumentado, J., and Simmonds, R. W. *Nature Physics* **11**(8), 635–639 August (2015).
- [14] Pirkkalainen, J.-M., Cho, S. U., Li, J., Paraoanu, G. S., Hakonen, P. J., and Sillanpää, M. A. *Nature* **494**(7436), 211–215 February (2013).
- [15] Pirkkalainen, J.-M., Cho, S., Massel, F., Tuorila, J., Heikkilä, T., Hakonen, P., and Sillanpää, M. *Nature Communications* **6**(1) November (2015).
- [16] Viennot, J., Ma, X., and Lehnert, K. *Physical Review Letters* **121**(18), 183601 October (2018).
- [17] Sletten, L. R., Moores, B. A., Viennot, J. J., and Lehnert, K. W. *Phys. Rev. X* **9**, 021056 Jun (2019).
- [18] O’Connell, A. D., Hofheinz, M., Ansmann, M., Bialczak, R. C., Lenander, M., Lucero, E., Neeley, M., Sank, D., Wang, H., Weides, M., Wenner, J., Martinis, J. M., and Cleland, A. N. *Nature* **464**(7289), 697–703 April (2010).
- [19] Chu, Y., Kharel, P., Yoon, T., Frunzio, L., Rakich, P. T., and Schoelkopf, R. J. *Nature* **563**(7733), 666 November (2018).
- [20] Arrangoiz-Arriola, P., Wollack, E. A., Wang, Z., Pechal, M., Jiang, W., McKenna, T. P., Witmer, J. D., Laer, R. V., and Safavi-Naeini, A. H. *Nature* **571**(7766), 537–540 July (2019).
- [21] Kounalakis, M., Blanter, Y. M., and Steele, G. A. *Physical Review Research* **2**(2) June (2020).
- [22] Koch, J., Yu, T. M., Gambetta, J., Houck, A. A., Schuster, D. I., Majer, J., Blais, A., Devoret, M. H., Girvin, S. M., and Schoelkopf, R. J. *Physical Review A* **76**(4), 042319 October (2007).
- [23] Xue, F., Wang, Y. D., Sun, C. P., Okamoto, H., Yamaguchi, H., and Semba, K. *New Journal of Physics* **9**(2), 35–35 February (2007).
- [24] Nation, P. D., Suh, J., and Blencowe, M. P. *Physical Review A* **93**(2), 022510 February (2016).
- [25] Khosla, K., Vanner, M., Ares, N., and Laird, E. *Physical Review X* **8**(2), 021052 May (2018).
- [26] Etaki, S., Poot, M., Mahboob, I., Onomitsu, K., Yamaguchi, H., and Zant, H. S. J. v. d. *Nature Physics* **4**(10), 785–788 October (2008).
- [27] Rodrigues, I. C., Bothner, D., and Steele, G. A. *Nature Communications* **10**(1) December (2019).
- [28] Schmidt, P., Amawi, M. T., Pogorzalek, S., Deppe, F., Marx, A., Gross, R., and Huebl, H. *arXiv:1912.08731 [cond-mat, physics:quant-ph]* December (2019). arXiv: 1912.08731.
- [29] Didier, N., Bourassa, J., and Blais, A. *Physical Review Letters* **115**(20), 203601 November (2015).
- [30] Leibfried, D., Blatt, R., Monroe, C., and Wineland, D. *Reviews of Modern Physics* **75**(1), 281–324 March (2003).
- [31] Barends, R., Kelly, J., Megrant, A., Sank, D., Jeffrey, E., Chen, Y., Yin, Y., Chiaro, B., Mutus, J., Neill, C., O’Malley, P., Roushan, P., Wenner, J., White, T. C., Cleland, A. N., and Martinis, J. M. *Physical Review Letters* **111**(8), 080502 August (2013).
- [32] Ludwig, M., Safavi-Naeini, A. H., Painter, O., and Marquardt, F. *Physical Review Letters* **109**(6), 063601 August (2012).
- [33] Bishop, L. S., Chow, J. M., Koch, J., Houck, A. A., Devoret, M. H., Thuneberg, E., Girvin, S. M., and Schoelkopf, R. J. *Nature Physics* **5**(2), 105–109 February (2009).
- [34] Touzard, S., Kou, A., Frattini, N., Sivak, V., Puri, S., Grimm, A., Frunzio, L., Shankar, S., and Devoret, M. *Physical Review Letters* **122**(8), 080502 February (2019).
- [35] Shevchenko, S. N., Ashhab, S., and Nori, F. *Physics Reports* **492**(1), 1–30 July (2010).

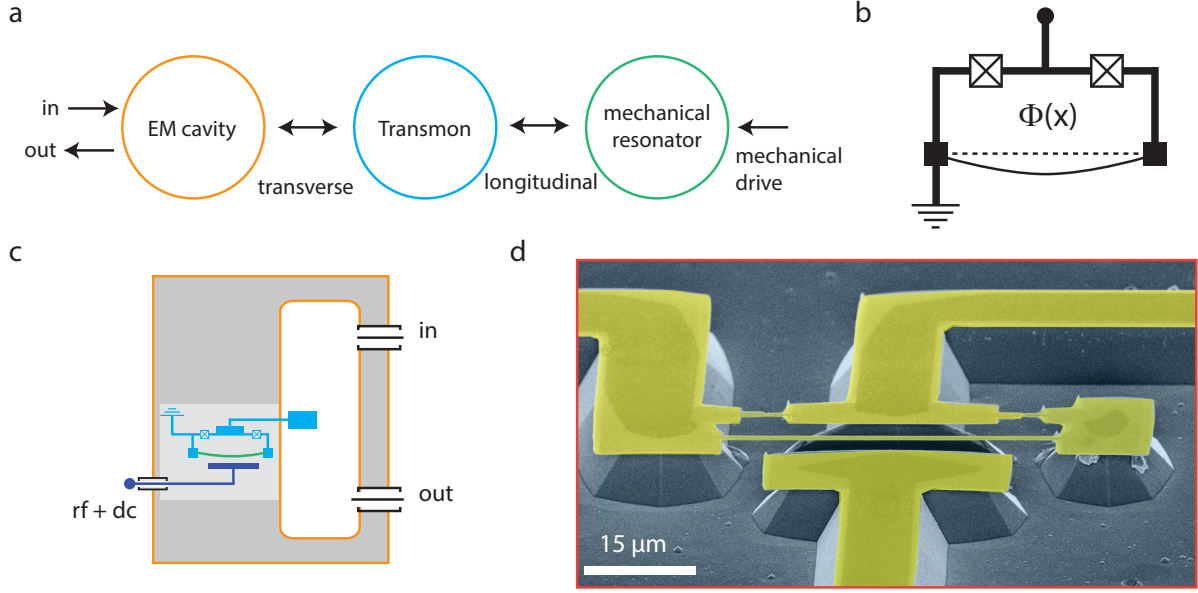


FIG. 1. (a) A schematic showing various components of the hybrid electromechanical system. The transmon qubit couples to an electromagnetic (EM) cavity via the transverse coupling. A low-frequency mechanical resonator couples to the transmon qubit via the longitudinal coupling. (b) A schematic of the SQUID loop with a suspended arm. Due to the magnetic flux $\Phi(x)$ dependence of Josephson inductance, it forms a displacement-dependent inductor. (c) A cross-sectional view of a 3D-cavity based transmon device. The gray (white) portion represents the copper (machined chamber). Input-output ports for microwave and a third port added for mechanical actuation is shown. The SQUID loop is placed inside a small recess of the cavity schematically shown by the lighter gray area. (d) A false-color SEM image of the SQUID loop, showing the suspended portion of the Josephson junctions and the nanobeam. The mechanical resonator has a length and width of 45 μm and 300 nm, respectively. It consists of a 50 nm coating of aluminum over 100 nm thick highly-stressed SiN film. The T-shaped electrode in the lower-half of the image is used to actuate the mechanical resonator.

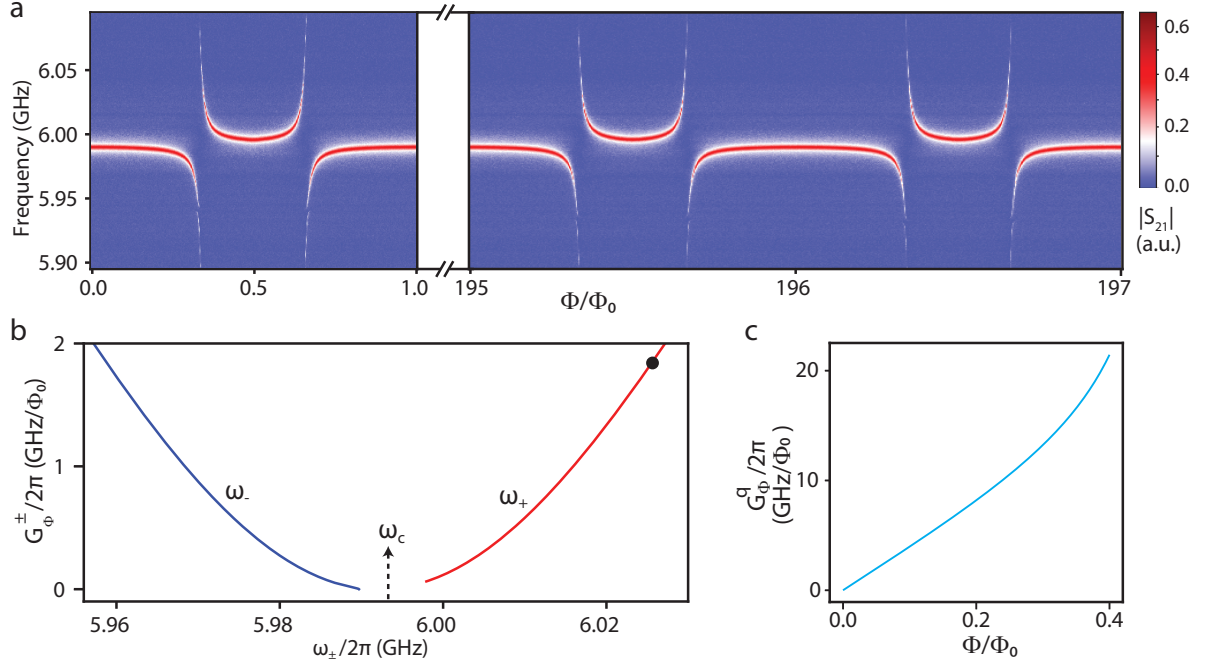


FIG. 2. (a) Color scale plot of transmission $|S_{21}|$ through the cavity as the magnetic flux through the SQUID loop is varied. The strong qubit-cavity coupling (J) manifests as the avoided-crossing, yielding $J \sim 2\pi \times 85$ MHz. The extension panel shows the trend of avoided crossing at larger values of the magnetic flux. (b) The flux-responsivity $G_{\Phi}^{\pm} = \partial\omega_{\pm}/\partial\Phi$, computed using the measured device parameters, assuming identical junctions, plotted as a function of hybridized frequencies. The black dot denotes the operating point of 6.025 GHz, corresponding to $G_{\Phi}^{+}/2\pi \sim 1.8$ GHz/ Φ_0 for the subsequent measurements. The arrow indicates the bare cavity frequency $\omega_c/2\pi \sim 5.993$ GHz. Panel (c) shows the flux-responsivity of uncoupled qubit $G_{\Phi}^q = \partial\omega_q/\partial\Phi$ with the magnetic flux.

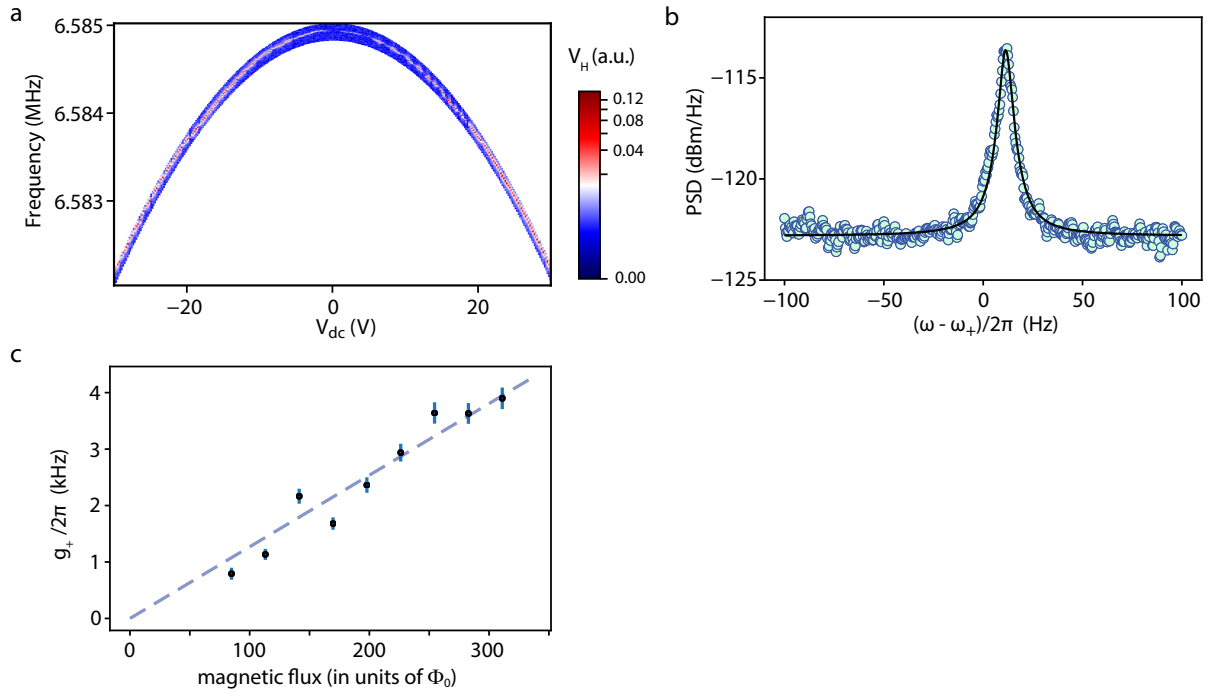


FIG. 3. (a) Color plot of the mixed-down signal V_H as mechanical actuation frequency and dc voltage is varied. The mechanical resonance appears as a sharp change in the color. Blue(red) color represents low(high) values of the signal. To reduce the total measurement time, the mechanical actuation frequency range is automatically adjusted to follow the mechanical mode. (b) Average PSD along with a fitted curve yielding a mechanical linewidth $\gamma_m \sim 2\pi \times 6$ Hz corresponding to a quality factor of $\sim 1.1 \times 10^6$. (c) Plot of the vacuum electromechanical coupling rate between hybridized-mode and the mechanical resonator as the magnetic flux through the SQUID loop is increased, while $\omega_+ = 2\pi \times 6.025$ GHz is kept fixed. The maximum flux applied corresponds to a field of 3.7 mT. The blue-dotted line shows the expected coupling rate calculated from the device parameters. The error bars represent the uncertainty resulting from the numerical fit of the power spectral density.

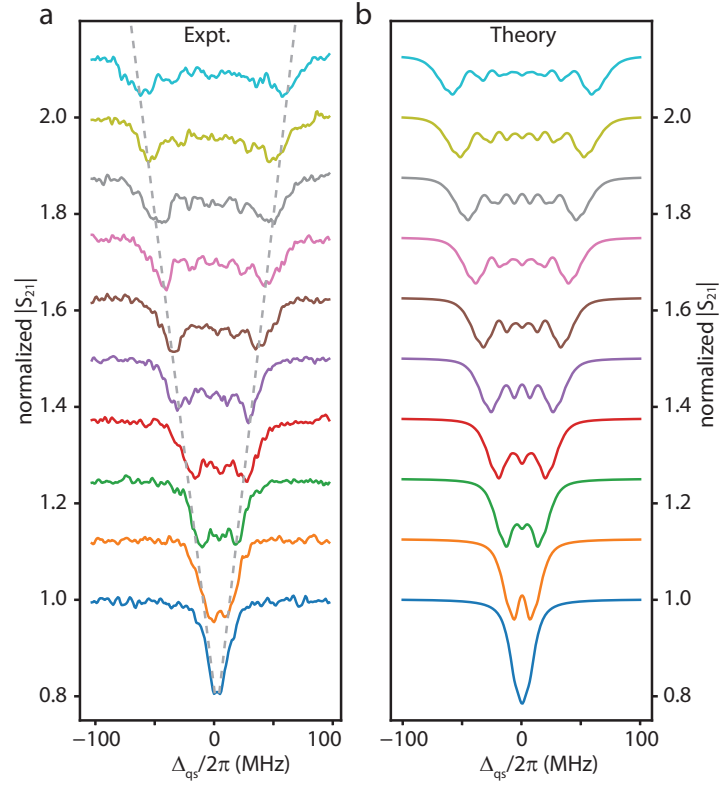


FIG. 4. (a) Measurement of the qubit spectrum with the detuning of spectroscopy tone $\Delta_{qs} = \omega_s - \omega_q$, where ω_s is the spectroscopy frequency. The mechanical drive signal is varied from 1 to 10 mV in steps of 1 mV (bottom to top). The Rabi flop rate $\Omega_R/2\pi$ is about 3 MHz. Apart from the primary splitting, weak fringes arising from the Landau-Zener-Stückelberg interference are visible. Dotted lines are added as guide to the eye. (b) Qubit spectrum calculated using the master equation. The qubit frequency deviation is changed from 7 MHz to 70 MHz in steps of 7 MHz (bottom to top). A qubit relaxation rate of 2 MHz, and a pure dephasing rate of 4 MHz is used to calculate the qubit spectrum. In both panels, the probe transmission corresponding to the lowest mechanical drive is normalized to one, and an offset of 0.125 has been added successively.

Supplementary Information: Large flux-mediated coupling in hybrid electromechanical system with a transmon qubit

Tanmoy Bera, Sourav Majumder, Sudhir Kumar Sahu, and Vibhor Singh*
Department of Physics, Indian Institute of Science, Bangalore-560012 (India)

Supplementary Note 1. Summary of device parameters

Table S1 lists some important device parameters.

Device parameters		
	Symbol	Value
Cavity dimension	$d_x \times d_y \times d_z$	$35 \times 35 \times 4 \text{ mm}^3$
Bare cavity frequency	$\omega_c/2\pi$	5.993 GHz
Maximum qubit frequency	$\omega_q^0/2\pi$	7.982 GHz
Qubit-cavity coupling rate	$J/2\pi$	85 MHz
Anharmonicity	$\alpha/2\pi$	-132 MHz
Room temperature junction resistance	R_n	3.67 k Ω
Josephson inductance of SQUID	L_J	4.6 nH
Junction capacitance	C_J	5 fF
Maximum Josephson energy	E_J^0/h	33.4 GHz
Charging energy from black-box simulation	E_C/h	255 MHz
Cavity impedance (simulation)	Z_c	0.6 Ω
Qubit impedance (simulation)	Z_q	275 Ω
SQUID loop area	A	$\sim 166 \text{ } \mu\text{m}^2$
Effective SQUID loop width (SQUID area / length of mechanical resonator)	w	$\sim 3.33 \text{ } \mu\text{m}$
SiN film thickness	d_1	100 nm
Al coating thickness	d_2	50 nm
Mechanical resonator length	l	$\sim 45 \text{ } \mu\text{m}$
Mechanical resonator width	b	300 nm
Mechanical resonator thickness	$d = (d_1 + d_2)$	150 nm
Tensile stress in SiN film	T	$\sim 2 \text{ GPa}$
Total mass of the mechanical resonator	m	$\sim 5.6 \text{ pg}$
Mechanical resonator frequency	$\omega_m/2\pi$	6.5849 MHz
Maximum applied magnetic field	B_{max}	3.7 mT

TABLE S1: Summary of parameters for the device studied in the main text

Supplementary Note 2. Device Fabrication and measurement setup:

The device is fabricated on a $5 \times 8 \text{ mm}^2$ silicon-(100) substrate coated with 100 nm highly pre-stressed SiN, deposited using LPCVD method. The entire design is patterned in a single electron-beam lithography step using a bilayer resist stack of LOR and PMMA. Subsequently, the shadow evaporation technique is used to deposit aluminum with an intermediate step of oxidation to realize tunnel Josephson junctions. Fig. S1(a) shows the optical image of the device after aluminum deposition.

To pattern the nanowire and release it from the substrate, we use two steps etching procedure. First, the exposed SiN is vertically etched by the reactive ion etching using SF_6 and CHF_3 plasma. The aluminum film naturally acts as a mask layer and thus protects the SiN underneath it. In the second step of etching, a modified TMAH based etchant is used to remove the exposed silicon while providing excellent selectivity against Al and SiN^{1,2}. For the etchant we prepare, the etch rate of Si along 100-direction is much faster than the 110- and 111-directions. Following wet-etching, the samples are thoroughly rinsed in DI water and IPA. The samples are then dried using a gentle blow of N_2 , without any critical-point drying. After the etch processes, we consistently observe a 30-50% increase in the room-temperature tunnel resistance of the junctions.

The fabricated sample is then placed inside a 3D copper cavity, machined out of OFHC copper (shown in Fig. S1(b)). Subsequently, the cavity assembly is cooled down to 25 mK in a dilution refrigerator. The copper cavity, along with

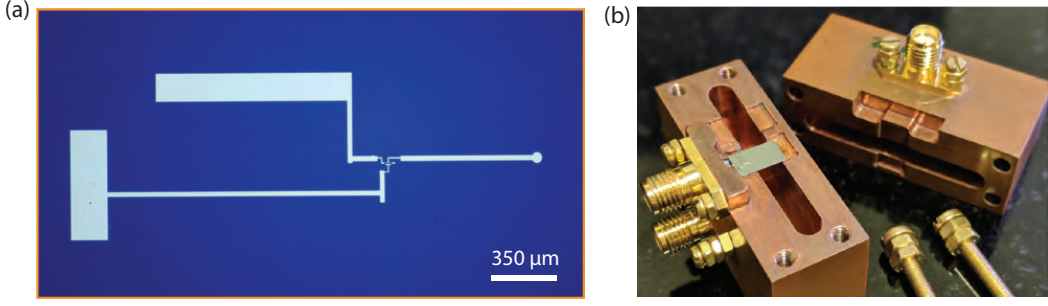


FIG. S1: (a) An optical image of the device before the silicon nitride (SiN) removal. The dark-blue color is due to 100 nm SiN coating over the Si substrate. (b) Image of the device placed in one half of the 3D waveguide cavity while the other half is placed beside. Wirebonds used to realize a single-ended qubit mode can be seen as well. The top SMA-port on the cavity-half showing two connectors is used for mechanical actuation.

a small solenoid, is kept inside a cryoperm-shield to protect from ambient magnetic field fluctuations. Fig. S2 shows the schematic of the complete measurement setup used in the experiment.

Supplementary Note 3. Device design simulation:

We use the black-box circuit quantization (BBQ) technique to simulate the design of the single-ended qubit³. We compute the imaginary part of the admittance Y_{sim} , as seen by the Josephson junction, with patterned substrate placed inside. For such computation, a lumped port is defined at the position of SQUID loop. The total reactive admittance, including the SQUID inductance and capacitance, is given by $Y_{\text{total}} = Y_{\text{sim}} + \omega C_J - \frac{1}{\omega L_J}$. Using the junction capacitance $C_J = 5$ fF and Josephson inductance $L_J = 7.5$ nH of the SQUID loop, the plot of Y_{total} and Y_{sim} is shown in Fig. S3(a). The zero-crossings with the positive slopes in Y_{total} denote the qubit and the cavity mode frequencies. By varying L_J , we identified the crossing on the right as the qubit mode.

The mechanical actuation electrode is designed in a way that the qubit relaxation rate through it can be kept lower, while maintaining sufficient actuation ability to drive the mechanical resonator. Apart from restricting the driveline within the cavity recess, we compute the qubit energy relaxation through the drive port. We simulate the qubit relaxation rate with and without the mechanical actuation electrode. The difference of two relaxation rates k_{leak} as a function of qubit frequency, is shown in Fig. S3(b).

Supplementary Note 4. Estimation of the mechanical resonator frequency:

The mechanical resonator is comprised of a highly pre-stressed (~ 2 GPa) SiN beam of thickness 100 nm, with 50 nm coating of aluminum on top. Using Euler-Bernoulli's beam theory⁴, the estimated frequency of the mechanical resonator is given by,

$$f_j = \frac{j^2 \pi}{2L^2} \sqrt{\frac{(EI)_{\text{eff}}}{(\rho A)_{\text{eff}}}} \sqrt{1 + \frac{(\sigma A)_{\text{eff}} L^2}{j^2 (EI)_{\text{eff}} \pi^2}}$$

where $j = 1, 2, 3, \dots$ denotes the vibrational mode index, L is the length of nano-beam and $(EI)_{\text{eff}}$, $(\sigma A)_{\text{eff}}$, and $(\rho A)_{\text{eff}}$ are the effective tensile stress, effective bending rigidity, and effective density respectively.

The effective density is given by,

$$(\rho A)_{\text{eff}} = \frac{\rho_1 d_1 + \rho_2 d_2}{d_1 + d_2} A = \rho A,$$

the effective bending rigidity is given by

$$(\sigma A)_{\text{eff}} = \frac{(\sigma_1 d_1 + \sigma_2 d_2)}{d_1 + d_2} A = \sigma A,$$

where $A = b (d_1 + d_2)$ is the cross sectional area of the mechanical resonator.

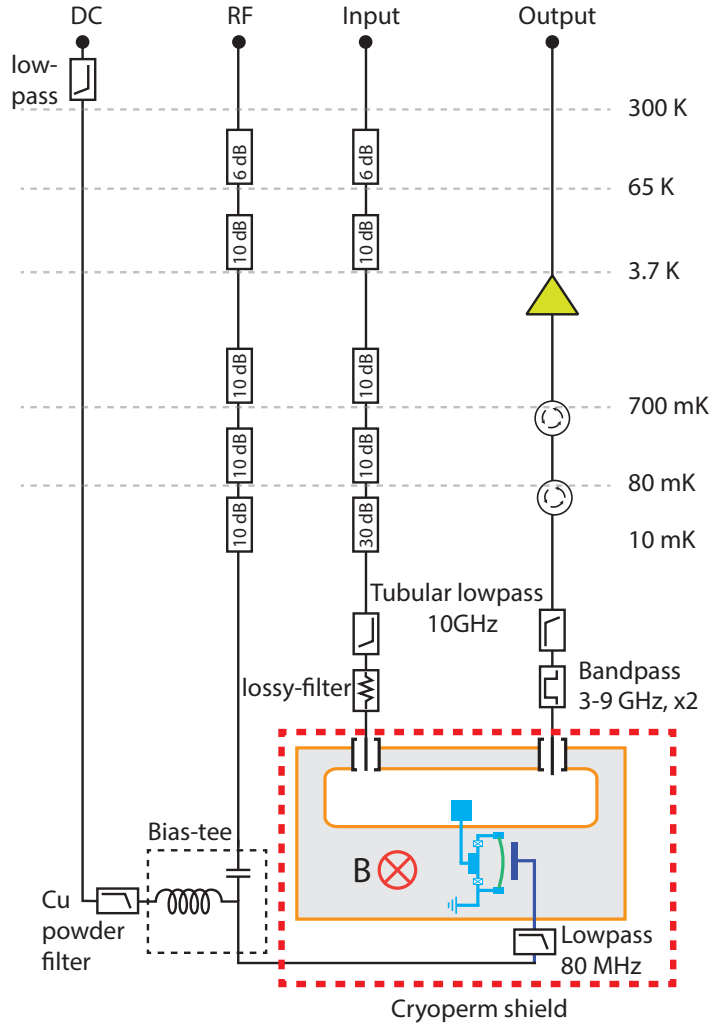


FIG. S2: Schematic of the measurement setup: The input line has 66 dB of cryogenic attenuation, where rf line has 46 dB of fixed attenuation. The bias-tee adds the rf and dc signals, which are used to actuate the mechanical oscillator. The cavity is kept inside a superconducting coil, use to apply the magnetic field B . A cryo-perm shield, shown as a red dashed rectangular box, encloses the sample and superconducting coil setup and provides very effective protection against the magnetic field fluctuations outside the fridge.

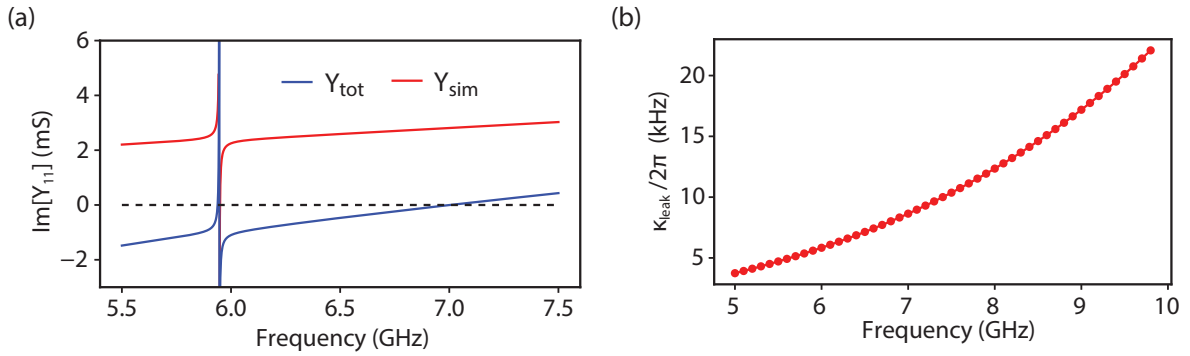


FIG. S3: (a) Admittance of the design computed using a finite element electromagnetic solver. Y_{sim} is the imaginary part of the admittance without the Josephson junction, and Y_{tot} is the imaginary part of the total admittance when the SQUID loop is present. (b) The qubit relaxation rate through the mechanical actuation port is plotted against the qubit frequency.

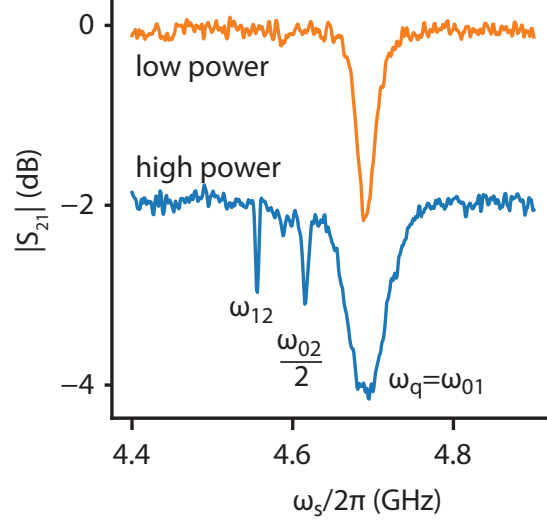


FIG. S4: Two-tone spectroscopy measurement of the qubit for two different spectroscopy powers. At low power, the dip represents the qubit transition from ground to the first excited state. With strong spectroscopy drive, the higher transitions become visible. An offset of -2 dB has been added to the data at the larger drive power to bring clarity.

The effective tensile stress for in-plane and out-of-plane mode is different. For the out-of-plane mode, it is given by

$$(EI)_{eff-oop} = b \frac{E_1^2 d_1^4 + 2E_1 E_2 d_2 (2d_1^3 + 2d_1 d_2^2 + 3d_1^2 d_2) + E_2^2 d_2^4}{12(E_1 d_1 + E_2 d_2)} = E_1 I_{eff}^{oop}.$$

Similarly, for the in-plane mode, it is given by,

$$(EI)_{eff-ip} = \frac{b^3(E_1 d_1 + E_2 d_2)}{12} = E_1 I_{eff}^{ip},$$

where b denotes the width of the mechanical resonator, d_1 and d_2 are the thickness of SiN and aluminium layers.

We use a Young's modulus of rigidity of $E_1 = 160$ GPa, tensile stress $\sigma_1 = 2$ GPa, and mass density $\rho_1 = 2800$ kg/m³ for SiN and $E_2 = 69$ GPa, density $\rho_2 = 2700$ kg/m³ for aluminum. The stress in aluminium film is negligible, and it does not affect the total tensile stress. Effectively, the aluminum coverage over SiN nanobeam increases the mass of the mechanical resonator, which leads to a decrease in the frequency. Using the parameters given above, we estimate the resonant frequency of the fundamental in-plane vibrational mode to be 7.7 MHz.

Supplementary Note 5. Measurement of the qubit anharmonicity:

We use the two-tone spectroscopy technique to measure the qubit anharmonicity. A weak probe near the cavity-frequency is used to continuously monitor transmission through the cavity, while a second spectroscopy tone ω_s near the qubit frequency is swept. When ω_s matches with allowed qubit transitions, the transmission through the cavity changes due to the dispersive coupling.

Fig. S4 shows the two-tone spectroscopy measurements at two different powers of the spectroscopy tone. At larger spectroscopy power, higher transition ω_{12} , and the two-photon transition ω_{02} become visible. We determine the qubit anharmonicity $\alpha \equiv \omega_{12} - \omega_q$ of $-2\pi \times 132$ MHz. It is important to mention that in a traditional 3D-transmon design, the qubit anharmonicity is approximately given by $-E_C$. Due to the modified design used here, the geometrical inductance of the wirebonds L_w dilutes the qubit anharmonicity.

In the limit, SQUID inductance $L_J \gg L_w$, the anharmonicity is given by⁵, $\alpha \approx -E_C/(1 + L_w/L_J)^3$. From the room temperature SQUID resistance measurement and finite element simulation of E_C we estimate $L_w \approx 1.13$ nH, and $L_J \approx 4.6$ nH.

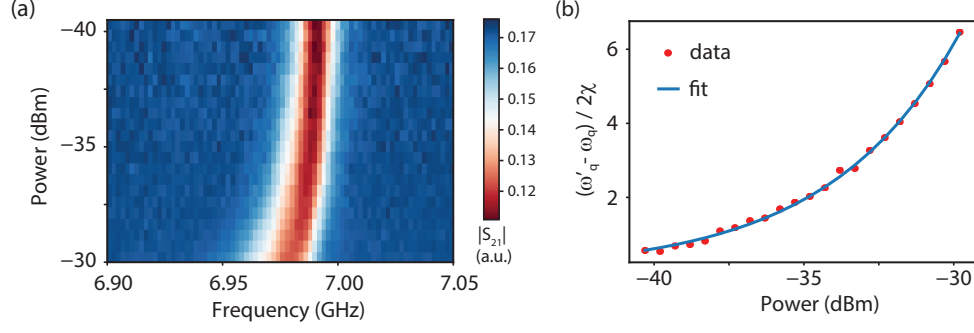


FIG. S5: (a) ac-Stark shift in two-tone spectroscopy: Plot of transmission through the cavity at dressed cavity frequency, while sweeping the spectroscopy frequency near the qubit transition with varying probe power. The red color represents the qubit transition. (b) Normalized qubit frequency shift, proportional to the number of intra-cavity photons, with increasing injected probe power.

Supplementary Note 6. ac-Stark shift and the calibration of the intra-cavity photons:

Fig. S5(a) shows the two-tone spectroscopy measurement when the qubit is dispersively detuned. The qubit transition frequency decreases with increasing probe power due to the photon-induced ac-Stark effect. The shifted qubit frequency is given by $\omega'_q = \omega_q + 2n\chi$, where n is the mean intra-cavity photon number⁶. We detune the qubit by ~ 1 GHz above the cavity mode near 6.992 GHz, and perform the two-tone spectroscopy measurements with varying probe power.

The dispersive shift is given by $\chi = J^2 \frac{\alpha}{\Delta(\Delta + \alpha)}$, where J is the coupling strength between the qubit and the cavity mode, α is the anharmonicity, and $\Delta = \omega_q - \omega_c$ is the qubit detuning. From the independent measurements of anharmonicity and qubit-cavity coupling, we compute the dispersive shift. The dispersive shift calculated this way, is then used to calibrate the number of intra-cavity photons.

The experimentally extracted intra-cavity photon number with increasing probe power from the signal generator, is plotted in Fig. S5(b). This allows us to estimate the total microwave attenuation of the input line (from the microwave signal generator to the input port of the cavity), estimated to be 79.7 dB.

Supplementary Note 7. Thermal motion and mechanical mode temperature calibration:

To determine the thermal occupation of the mechanical resonator, we operate the system at $\omega_+/2\pi = 6.025$ GHz. While pumping this mode with a cw-tone at 6.025 GHz, we measure the total integrated power P_m in lower sideband. Also, the transmitted power P_d at the carrier frequency ω_+ is recorded. To eliminate the records made during any flux-jump event, we record the transmission $|S_{21}|$ before and after every trace measured by the spectrum analyzer. While we take this precaution, it is worth pointing out that all the data shown in the main manuscript is from the measurements runs, where we did not observe any flux-jump. Fig. S6(a) shows a 2D color-map of 200 traces of the power spectral density (PSD) measured with a spectrum analyzer. A plot of $|S_{21}|$ (at ω_+) for all the 200 traces is shown in Fig. S6(b).

Fig. S6(c) and (d) show the average trace of lower-sideband noise spectra measured at 25 mK and 50 mK, respectively. The down-converted power at the lower sideband frequency for zero detuning driving is given by $P_m = P_d (g_+ / (\kappa^2/4 + \omega_m^2)) n_m^{th}$.

Device parameter	$T = 25$ mK	$T = 50$ mK
Transmitted power at carrier frequency P_d	-75.9 dBm	-77.3 dBm
Cavity dissipation rate $\kappa/2\pi$	4.1 MHz	5.1 MHz

TABLE S2: System parameters used for the calibration of phonon occupancy

Assuming the vacuum coupling rate to be the same for two temperatures, from the results shown in Fig. S6(c), (d) and the parameter values in Table S2, we find the ratio $n_m^{25}/n_m^{50} \approx 1$. This led us to conclude that the mechanical resonator is thermalized to 50 mK or a higher temperature. The vacuum coupling rate, shown in Fig. 3(c) of the

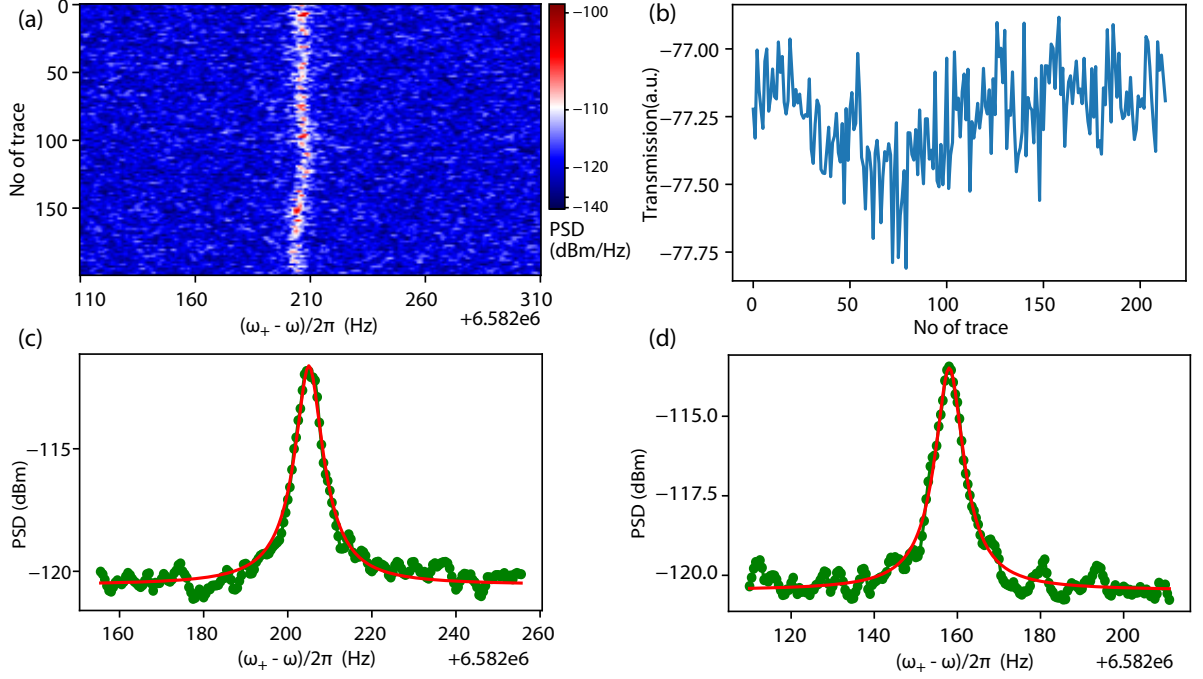


FIG. S6: (a) A color plot of 200 power spectral density traces. (b) Cavity transmission $|S_{21}(\omega_+)|$ during the measurement shown in (a). The transmission value is checked before initiating the PSD trace and validated after the PSD trace is over. (c) and (d) show the average power spectral density at the lower sideband measured at 25 and 50 mK, respectively. The dressed mode is driven with a mean photon occupation of 0.2 at 6.025 GHz.

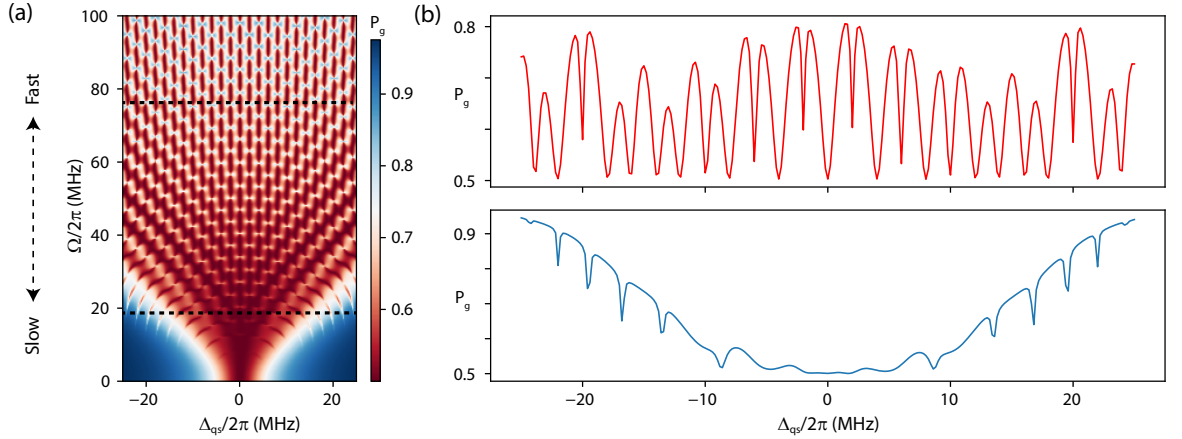


FIG. S7: (a) The LZS interference pattern with increasing qubit frequency deviation. The time-averaged value of $P_g = (1 - \langle \hat{\sigma}_z \rangle)/2$ is plotted with respect to detuning Δ_{qs} . (b) The top (bottom) plot shows the response for high (low) values of qubit frequency deviation. The linecuts are taken at $\Omega/2\pi = 76$ MHz (top) and 18 MHz (bottom), indicated by the black dashed line in the color plot. The calculations were done using $\Omega_R/2\pi = 8$ MHz, $\omega_m/2\pi = 2$ MHz and $\gamma_1/2\pi = 0.1$ MHz.

main text, has been calculated assuming a thermalization to 53 mK as these values fall roughly on the estimated values of g_+ from the device parameters.

Supplementary Note 8. Theoretical Model to understand Landau-Zener-Stückelberg (LSZ) interference:

When the qubit is detuned far away from the cavity, the total Hamiltonian of the system can be written as⁶,

$$H^{dis} = \hbar\omega_c \hat{a}^\dagger \hat{a} + \frac{\hbar\omega_q}{2} \hat{\sigma}_z + \hbar\omega_m \hat{b}^\dagger \hat{b} + \hbar\chi \hat{\sigma}_z \hat{a}^\dagger \hat{a} + \hbar g_{qm} \hat{\sigma}_z (\hat{b} + \hat{b}^\dagger) \quad (S1)$$

Due to a large difference between the qubit and mechanical resonator frequency, and g_{qm} being much smaller than the qubit frequency, we invoke the adiabatic approximation. A coherent drive on the mechanical resonator effectively results in a frequency-modulated qubit. The effective Hamiltonian can be written as,

$$H = \hbar\omega_c \hat{a}^\dagger \hat{a} + \frac{\hbar(\omega_q + \Omega \sin(\omega_m t))}{2} \hat{\sigma}_z + \hbar\omega_m \hat{b}^\dagger \hat{b} + \hbar\chi \hat{\sigma}_z \hat{a}^\dagger \hat{a} \quad (S2)$$

where $\Omega = g_{qm}\epsilon_m/x_{zp}$ is the qubit frequency deviation, and ϵ_m is the mechanical amplitude. Due to the longitudinal coupling, the mechanical resonator only contributes to the modulation of the qubit frequency.

To simulate the two-tone spectroscopy data (main text Fig.4), we add probe and spectroscopy drives to the Hamiltonian. After performing the rotating frame transformation at the spectroscopy frequency ω_s and the probe frequency, we get an effective Hamiltonian given by,

$$H = \frac{\hbar(\Delta_{qs} + \Omega \sin(\omega_m t))}{2} \hat{\sigma}_z + \hbar\chi(1 + \hat{\sigma}_z) \hat{a}^\dagger \hat{a} + \epsilon_{probe}(\hat{a} + \hat{a}^\dagger) + \frac{\Omega_R}{2} \hat{\sigma}_x, \quad (S3)$$

where $\Delta_{qs} = \omega_q - \omega_s$, ϵ_{probe} is the amplitude of the probe signal, and Ω_R is the amplitude of the spectroscopy signal (the Rabi-flop rate).

The time evolution of different operators can be calculated by using the master equation solver of the QuTip package⁷. We solve for the steady-state of $\langle \hat{a} \rangle_{ss}$ using the total Hamiltonian and define the transmission as the ratio of the time-averaged value of $\langle \hat{a} \rangle_{ss}$ to the probe amplitude *i.e.* $S_{21} = \langle \hat{a} \rangle_{ss} / \epsilon_{probe}$. Spectroscopy signal was varied near the qubit transition, while the probe signal frequency was kept fixed at the dressed cavity frequency corresponding to the qubit being in the ground state. Their amplitudes were kept constant during simulation *i.e.* $\Omega_R/2\pi = 3$ MHz and $\epsilon_{probe}/2\pi = 10$ kHz. We use a dispersive shift $\chi/2\pi = -0.71$ MHz. The results from such calculations are plotted as the solid lines in Fig. 4(b) of the main text.

In the two-tone spectroscopy measurements, the measured signal is directly related to $\langle \hat{\sigma}_z \rangle$. Therefore, the spectrum can also be worked out using the Hamiltonian of the qubit subspace only. The model, therefore, can be simplified to a two-level system (TLS), which is driven along the longitudinal direction (by the mechanical motion) and along the transverse direction (by the spectroscopy tone) simultaneously. In a frame rotating at the spectroscopy frequency, the Hamiltonian can be written as,

$$H_{TLS} = \frac{\Delta_{qs} + \Omega \sin(\omega_m t)}{2} \hat{\sigma}_z + \frac{\Omega_R}{2} \hat{\sigma}_x. \quad (S4)$$

The time evolution of the system can be worked out by using the Lindblad master equation,

$$\dot{\rho} = -\frac{i}{\hbar} [H_{TLS}, \rho] + \gamma_1 \mathcal{D}[\hat{\sigma}_-]\rho + \frac{\gamma_\phi}{2} \mathcal{D}[\hat{\sigma}_z]\rho, \quad (S5)$$

where γ_1 and γ_ϕ are the qubit relaxation and the qubit pure dephasing rates, respectively and the Lindblad superoperator $\mathcal{D}[\hat{F}]$ is defined as,

$$\mathcal{D}[\hat{F}]\rho = \hat{F}\rho\hat{F}^\dagger - \frac{1}{2}\hat{F}^\dagger\hat{F}\rho - \frac{1}{2}\rho\hat{F}^\dagger\hat{F}. \quad (S6)$$

This leads to a set of equation of motion as:

$$\frac{d}{dt} \langle \hat{\sigma}_x \rangle = -(\Delta_{qs} + \Omega \sin(\omega_m t)) \langle \hat{\sigma}_y \rangle - \left(\frac{\gamma_1}{2} + \gamma_\phi \right) \langle \hat{\sigma}_x \rangle \quad (S7a)$$

$$\frac{d}{dt} \langle \hat{\sigma}_y \rangle = -\Omega_R \langle \hat{\sigma}_z \rangle + (\Delta_{qs} + \Omega \sin(\omega_m t)) \langle \hat{\sigma}_x \rangle - \left(\frac{\gamma_1}{2} + \gamma_\phi \right) \langle \hat{\sigma}_y \rangle \quad (S7b)$$

$$\frac{d}{dt}\langle\hat{\sigma}_z\rangle = \Omega_R\langle\hat{\sigma}_y\rangle - \gamma_1(1 + \langle\hat{\sigma}_z\rangle) \quad (\text{S7c})$$

We compute the steady-state value of $\langle\hat{\sigma}_z\rangle$ by numerically integrating the Equation S7. To replicate the measurements, we vary the spectroscopy frequency near the ω_q (Δ_{qs}) and strength of the modulation Ω and plot the steady state value of $(1 - \langle\hat{\sigma}_z\rangle)/2$.

Fig. S7 shows the result from the numerical calculations showing the characteristic Landau-Zener-Stückelberg (LZS) interference pattern⁸. In the limit of fast-passage across the avoided crossing ($\Omega_R \ll \Omega\omega_m/\Omega_R$), the interference fringes are separated by the modulation frequency ω_m . In the slow-passage limit ($\Omega_R \gtrsim \Omega\omega_m/\Omega_R$), as the system undergoes the avoided crossing, the probability of diabatic transition increases, and the separation between the fringes is no longer solely determined by ω_m .

Splitting of the qubit spectrum can also be understood from a semi-classical model. In this approach, we calculate the time averaged value of $\langle\hat{\sigma}_z\rangle$ when qubit frequency is being modulated at ω_m , thereby asserting that adiabatic approximation.

Using Eq. S7, the steady state value of $\langle\hat{\sigma}_z\rangle$ can be obtained as

$$\langle\hat{\sigma}_z\rangle = -1 + \frac{\Omega_R^2 \frac{\gamma_2}{\gamma_1}}{\gamma_2^2 + \Omega_R^2 \frac{\gamma_2}{\gamma_1} + [\Delta_{qs} + \Omega \sin(\omega_m t)]^2}, \quad (\text{S8})$$

where $\gamma_2 = (\frac{\gamma_1}{2} + \gamma_\phi)$. We define the time averaged value of $\langle\hat{\sigma}_z\rangle$ as,

$$\overline{\langle\hat{\sigma}_z\rangle} = \frac{1}{T} \int_0^T \langle\hat{\sigma}_z\rangle dt, \quad (\text{S9})$$

where $T = 2\pi/\omega_m$ is the time period of the mechanical oscillation. Therefore,

$$\overline{\langle\hat{\sigma}_z\rangle} = -1 + \frac{\Omega_R^2 \frac{\gamma_2}{\gamma_1}}{T} \int_0^T \frac{dt}{\gamma_2^2 + \Omega_R^2 \frac{\gamma_2}{\gamma_1} + [\Delta_{qs} + \Omega \sin(\frac{2\pi t}{T})]^2}. \quad (\text{S10})$$

To carry out the integral, we first scale the time variable and then recast the integral as,

$$\overline{\langle\hat{\sigma}_z\rangle} = -1 - \frac{\Omega_R^2 \frac{\gamma_2}{\gamma_1}}{2\pi \sqrt{\gamma_2^2 + \Omega_R^2 \frac{\gamma_2}{\gamma_1}}} \text{Im} \left[\int_0^{2\pi} \frac{dx}{i \sqrt{\gamma_2^2 + \Omega_R^2 \frac{\gamma_2}{\gamma_1} + \Delta_{qs} + \Omega \sin(x)}} \right] \quad (\text{S11})$$

This integral can be transformed into a function of a complex variable and solved using Cauchy's integral formula with a contour described by $|z| = 1$. The important part of the calculation is the fact that for any value of Δ_{qs} , there is only one pole that exists inside the contour. Using the residue theorem, the final answer can be written as,

$$\overline{\langle\hat{\sigma}_z\rangle} = -1 + \frac{\Omega_R^2 \frac{\gamma_2}{\gamma_1}}{\beta} \left| \sin\left(\frac{\theta}{2}\right) \right|, \quad (\text{S12})$$

$$\beta = \sqrt{\gamma_2^2 + \Omega_R^2 \frac{\gamma_2}{\gamma_1}} \sqrt[4]{\left(\Delta_{qs}^2 - \gamma_2^2 - \Omega_R^2 \frac{\gamma_2}{\gamma_1} - \Omega^2\right)^2 + 4\Delta_{qs}^2 \left(\gamma_2^2 + \Omega_R^2 \frac{\gamma_2}{\gamma_1}\right)} \quad (\text{S13})$$

and

$$\theta = \tan^{-1} \left[\frac{2\Delta_{qs} \sqrt{\gamma_2^2 + \Omega_R^2 \frac{\gamma_2}{\gamma_1}}}{\Delta_{qs}^2 - \gamma_2^2 - \Omega_R^2 \frac{\gamma_2}{\gamma_1} - \Omega^2} \right] \quad (\text{S14})$$

Using the decoupled cavity-Bloch equation in the steady state, the normalized transmission through the cavity can be written as,

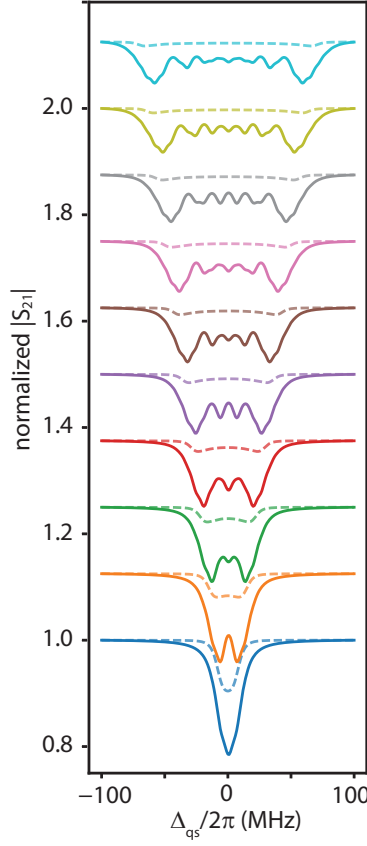


FIG. S8: The solid lines show the results from the Master equation. The dotted lines show the results from semi-classical calculation. Clearly the calculations performed using the Master equation matches the experimental results better. The calculations were done using the same parameters as used for Fig-4 shown in the main text.

$$S_{21} = \frac{-i\kappa/2}{\kappa/2 + i\chi \left(1 + \langle \hat{\sigma}_z \rangle\right)} \quad (\text{S15})$$

Figure S8 shows the qubit spectrum using Eq. S15. For comparison, solution obtained from the Master equation have been included as well.

* Electronic address: v.singh@iisc.ac.in

¹ Yan, G., Chan, P. C. H., Hsing, I.-M., Sharma, R. K., Sin, J. K. O., and Wang, Y. *Sensors and Actuators A: Physical* **89**(1), 135–141 March (2001).

² Norte, R. A. *Nanofabrication for On-Chip Optical Levitation, Atom-Trapping, and Superconducting Quantum Circuits*. phd, California Institute of Technology, (2015).

³ Nigg, S. E., Paik, H., Vlastakis, B., Kirchmair, G., Shankar, S., Frunzio, L., Devoret, M. H., Schoelkopf, R. J., and Girvin, S. M. *Physical Review Letters* **108**(24), 240502 June (2012).

⁴ Seitner, M. J., Gajo, K., and Weig, E. M. *Applied Physics Letters* **105**(21), 213101 November (2014).

⁵ Chen, Y., Neill, C., Roushan, P., Leung, N., Fang, M., Barends, R., Kelly, J., Campbell, B., Chen, Z., Chiaro, B., Dunsworth, A., Jeffrey, E., Megrant, A., Mutus, J., O'Malley, P., Quintana, C., Sank, D., Vainsencher, A., Wenner, J., White, T., Geller, M. R., Cleland, A., and Martinis, J. M. *Physical Review Letters* **113**(22), 220502 November (2014).

⁶ Koch, J., Yu, T. M., Gambetta, J., Houck, A. A., Schuster, D. I., Majer, J., Blais, A., Devoret, M. H., Girvin, S. M., and Schoelkopf, R. J. *Physical Review A* **76**(4), 042319 October (2007).

⁷ Johansson, J. R., Nation, P. D., and Nori, F. *Computer Physics Communications* **183**(8), 1760–1772 August (2012).

⁸ Shevchenko, S. N., Ashhab, S., and Nori, F. *Physics Reports* **492**(1), 1–30 July (2010).